Nuclear symmetry energy and hadron-quark mixed phase in neutron stars

X. H. Wu and H. Shen[*]

School of Physics, Nankai University, Tianjin 300071, China

We study the hadron-quark mixed phase, which may occur in the interior of neutron stars. The relativistic mean-field model is employed to describe the hadronic phase, while the Nambu-Jona-Lasinio model is used for the quark phase. We examine the effects of nuclear symmetry energy in the hadronic phase and repulsive vector interaction in the quark phase. For the treatment of hadron-quark mixed phase, we describe and compare four methods: (1) energy minimization method, (2) coexisting phases method, (3) Gibbs construction, and (4) Maxwell construction. The finite-size effects like surface and Coulomb energies are taken into account in the energy minimization and coexisting phases methods, which play a key role in determining the pasta configuration during the hadron-quark phase transition. It is found that massive neutron stars may contain hadron-quark pasta phases, but pure quark matter is unlikely to occur in the interior of neutron stars.

I. INTRODUCTION

Neutron stars are ideal laboratories for the study of dense matter. In the core of neutron stars, exotic phases like deconfined quarks may be present [1–3]. Over the past decades, there have been numerous research works concerning the hadron-quark phase transition in neutron stars [4–14]. In most of the studies, Gibbs construction [4] and/or Maxwell construction are commonly used for the description of hadron-quark mixed phases. In the Maxwell construction, local charge neutrality is imposed, and furthermore coexisting hadronic and quark phases have equal pressures and baryon chemical potentials but different electron chemical potentials. However, in the Gibbs construction, only global charge neutrality is required, so hadronic and quark phases are allowed to be charged separately and have continuous chemical potentials. It is well known that Gibbs and Maxwell constructions correspond respectively to the two limits of zero and very large surface tension at the hadron-quark interface, and therefore, the mixed phase with the Gibbs construction has lower energy than the one with the Maxwell construction. It was reported in Ref. [15] that there are significant differences in the behavior of compact stars between the Gibbs and Maxwell constructions. It is noticeable that both Gibbs and Maxwell constructions involve only bulk contributions, where the finite-size effects like surface and Coulomb energies are neglected. When surface and Coulomb energies are considered, a hadron-quark mixed phase with pasta structures is expected to occur [16–21]. The geometric configuration in the mixed phase may change from droplet to rod, slab, tube, and bubble with increasing baryon density [17–20]. It is interesting to examine how the hadron-quark mixed phase can be affected by different treatment methods.

To describe hadron-quark pasta phases, we use the Wigner-Seitz approximation, where the system is divided into periodically repeating charge-neutral cells. The hadronic and quark phases inside the cell are assumed to be separated by a sharp interface with a finite surface tension. It is known that the surface tension plays a key role in determining the structure of hadron-quark mixed phase [16–21], but its value is poorly known so far. The calculation in the MIT bag model by using the multiple reflection expansion (MRE) method predicted a value of the surface tension $\sigma \approx 10$ MeV/fm^2 [22], while recent calculations within the MRE framework show that the surface tension falls in the range of 2 to 20 MeV/fm^2 for baryon densities between 2 to 10 times the nuclear saturation density [23,24]. A similar calculation in the Nambu-Jona-Lasinio (NJL) model including color superconductivity yielded $\sigma \approx 145$–165 MeV/fm^2 [25]. The surface tension calculated from a geometric approach fell in the range $\sigma \approx 7$–30 MeV/fm^2 [26]. Due to the uncertainty of σ, we treat the surface tension as a free parameter in the present work. We employ the three-flavor NJL model to describe quark matter, while the relativistic mean-field (RMF) models are adopted for hadronic matter. The NJL model has been widely used as an effective theory of QCD for the description of quark matter [9,27–31], since it can successfully describe dynamical chiral symmetry breaking and generation of constituent quark masses. In this work, we use the NJL model including repulsive vector interactions. It has been reported in the literature that including repulsive vector interactions could significantly affect the QCD phase diagram [32–34] and stiffen the equation of state (EOS) of quark matter [19,20,35–41].

For the description of hadronic matter, we employ two successful RMF models, namely TM1 [42] and IUFSU [43], which could provide good descriptions of finite nuclei and acceptable maximum mass of neutron stars. The TM1 model has been successfully applied in constructing the EOS for supernova simulations and neutron stars [44,45]. The

————
[*]shennankai@gmail.com

IUFSU model, which was proposed to overcome a smaller neutron-star mass predicted by the FSU model, has also been used for the study of neutron-star structure [47–49]. Both of these models include nonlinear terms for σ and ω mesons, while the IUFSU model includes an additional ω-ρ coupling term that plays a crucial role in determining the density dependence of symmetry energy and affecting the neutron-star structure [43,46–50]. It is well known that nuclear symmetry energy $E_{\rm sym}$ and its slope L play an important role in understanding many phenomena in nuclear physics and astrophysics [51–57]. Especially, neutron-star radii and crust structures are closely related to the symmetry energy slope L [47–50]. Recently, many efforts have been devoted to constraining the values of $E_{\rm sym}$ and L at saturation density based on astrophysical observations and terrestrial nuclear experiments [58–65]. In Refs. [57,58], a sufficient number of constraints on the symmetry energy parameters have been summarized, and the most probable values for the symmetry energy and its slope at saturation density were found to be $E_{\rm sym} = 31.7 \pm 3.2$ MeV and $L = 58.7 \pm 28.1$ MeV, respectively, with a much larger error for L than that for $E_{\rm sym}$. Although the TM1 and IUFSU models give similar binding energies of finite nuclei, their symmetry energy slopes are very different from each other ($L = 47.2$ MeV in IUFSU and $L = 110.8$ MeV in TM1). In order to examine the L dependence of hadron-quark pasta phases, we employ two sets of generated models based on the TM1 and IUFSU parametrizations as described in Ref. [66]. The models in each set were obtained by simultaneously adjusting g_ρ and $\Lambda_{\rm v}$ so as to achieve a given L at saturation density n_0 while keeping $E_{\rm sym}$ fixed at the baryon density $n_b = 0.11$ fm^{-3}. The choice of fixing symmetry energy at $n_b = 0.11$ fm^{-3} aims to produce similar binding energies of finite nuclei within one set of generated models, which should be consistent with experimental data. It is noticeable that all models in each set have the same isoscalar saturation properties and fixed symmetry energy $E_{\rm sym}$ at $n_b = 0.11$ fm^{-3} but have different symmetry energy slope L. By using a set of models with different values of L, it is possible to study the effects of nuclear symmetry energy on the hadron-quark phase transition and pasta structures in neutron stars.

The main purpose of this article is to investigate the properties of hadron-quark pasta phases, which could be affected by nuclear symmetry energy and other parameters such as the surface tension σ and vector coupling G_V in the NJL model. To describe the hadron-quark pasta phase, we use the energy minimization (EM) method, where the equilibrium state at a given baryon density is determined by minimizing the total energy density. The EM method, which is referred to as the compressible liquid-drop (CLD) model, has been widely used in the study of nuclear liquid-gas phase transition at subnuclear densities [66–69]. In the EM method, the equilibrium conditions for coexisting phases are derived by minimization of the total energy including surface and Coulomb contributions, which are different from the Gibbs conditions without finite-size effects. Furthermore, a simple coexisting phases (CP) method [48,70] is also used and compared for the description of hadron-quark pasta phases. In the CP method, two coexisting phases satisfy the Gibbs conditions for phase equilibrium, which require equal pressures and chemical

potentials for two phases [4–12]. After the equilibrium state is obtained by applying the Gibbs conditions, the surface and Coulomb energies are perturbatively taken into account in the CP method. Since the equilibrium conditions in the EM method are derived by minimization of the total energy including surface and Coulomb contributions, the finite-size effects are treated relatively well in the EM method. By comparing results from different treatments, we can examine how the pasta structures could be influenced by the method used in the calculations.

This article is organized as follows. In Sec. II, we briefly describe the RMF models for hadronic matter and discuss the choice of parameters. In Sec. III, the NJL model used for quark matter is briefly introduced. In Sec. IV, we describe and compare the four methods used for the study of hadron-quark mixed phase, namely (1) EM method, (2) CP method, (3) Gibbs construction, and (4) Maxwell construction. In Sec. V, we show numerical results and discuss the properties of hadron-quark mixed phase in neutron stars. The effects of nuclear symmetry energy and model dependence are also examined. Section VI is devoted to the conclusions.

II. HADRONIC MATTER PHASE

The hadronic matter is described by the RMF model, where nucleons interact via the exchange of isoscalar-scalar meson σ, isoscalar-vector meson ω, and isovector-vector meson ρ. For hadronic matter consisting of nucleons (p and n) and leptons (e and μ), the Lagrangian density is written as

$$
\begin{aligned}
\mathcal{L}_{\rm RMF} = & \sum_{i=p,n} \bar{\psi}_i \Big\{ i\gamma_\mu \partial^\mu - (M + g_\sigma \sigma) \\
& - \gamma_\mu \Big[g_\omega \omega^\mu + \frac{g_\rho}{2} \tau_a \rho^{a\mu} \Big] \Big\} \psi_i \\
& + \frac{1}{2} \partial_\mu \sigma \partial^\mu \sigma - \frac{1}{2} m_\sigma^2 \sigma^2 - \frac{1}{3} g_2 \sigma^3 - \frac{1}{4} g_3 \sigma^4 \\
& - \frac{1}{4} W_{\mu\nu} W^{\mu\nu} + \frac{1}{2} m_\omega^2 \omega_\mu \omega^\mu + \frac{1}{4} c_3 (\omega_\mu \omega^\mu)^2 \\
& - \frac{1}{4} R^a_{\mu\nu} R^{a\mu\nu} + \frac{1}{2} m_\rho^2 \rho^a_\mu \rho^{a\mu} \\
& + \Lambda_{\rm v} \big(g_\omega^2 \omega_\mu \omega^\mu \big) \big(g_\rho^2 \rho^a_\mu \rho^{a\mu} \big) \\
& + \sum_{l=e,\mu} \bar{\psi}_l (i\gamma_\mu \partial^\mu - m_l) \psi_l,
\end{aligned}
\tag{1}
$$

where $W^{\mu\nu}$ and $R^{a\mu\nu}$ are the antisymmetric field tensors corresponding to ω^μ and $\rho^{a\mu}$, respectively. In the RMF approach, the meson fields are treated as classical fields and the field operators are replaced by their expectation values. For a static system, the nonvanishing expectation values are $\sigma = \langle \sigma \rangle$, $\omega = \langle \omega^0 \rangle$, and $\rho = \langle \rho^{30} \rangle$.

In uniform hadronic matter, the equations of motion for meson mean fields have the following form:

$$
m_\sigma^2 \sigma + g_2 \sigma^2 + g_3 \sigma^3 = -g_\sigma \big(n_p^s + n_n^s \big),
\tag{2}
$$

$$
m_\omega^2 \omega + c_3 \omega^3 + 2\Lambda_{\rm v} g_\omega^2 g_\rho^2 \rho^2 \omega = g_\omega (n_p + n_n),
\tag{3}
$$

$$
m_\rho^2 \rho + 2\Lambda_{\rm v} g_\omega^2 g_\rho^2 \omega^2 \rho = \frac{g_\rho}{2} (n_p - n_n),
\tag{4}
$$

TABLE I. Parameter sets TM1 and IUFSU for the RMF Lagrangian. All masses are in MeV.

Model	M	m_σ	m_ω	m_ρ	g_σ	g_ω	g_ρ	g_2 (fm^{-1})	g_3	c_3	Λ_v
TM1	938.0	511.198	783.0	770.0	10.0289	12.6139	9.2644	−7.2325	0.6183	71.3075	0.000
IUFSU	939.0	491.500	782.5	763.0	9.9713	13.0321	13.5900	−8.4929	0.4877	144.2195	0.046

where n_i^s and n_i denote the scalar and number densities of species i, respectively. The energy density of hadronic matter is given by

$$
\begin{aligned}
\varepsilon_{\rm HP} = & \sum_{i=p,n} \frac{1}{\pi^2} \int_0^{k_F^i} \sqrt{k^2 + M^{*2}}\, k^2 dk \\
& + \frac{1}{2} m_\sigma^2 \sigma^2 + \frac{1}{3} g_2 \sigma^3 + \frac{1}{4} g_3 \sigma^4 + \frac{1}{2} m_\omega^2 \omega^2 \\
& + \frac{3}{4} c_3 \omega^4 + \frac{1}{2} m_\rho^2 \rho^2 + 3\Lambda_v \big(g_\omega^2 \omega^2\big)\big(g_\rho^2 \rho^2\big) \\
& + \sum_{l=e,\mu} \frac{1}{\pi^2} \int_0^{k_F^l} \sqrt{k^2 + m_l^2}\, k^2 dk,
\end{aligned}
\tag{5}
$$

and the pressure is written as

$$
\begin{aligned}
P_{\rm HP} = & \sum_{i=p,n} \frac{1}{3\pi^2} \int_0^{k_F^i} \frac{k^4 dk}{\sqrt{k^2 + M^{*2}}} \\
& - \frac{1}{2} m_\sigma^2 \sigma^2 - \frac{1}{3} g_2 \sigma^3 - \frac{1}{4} g_3 \sigma^4 + \frac{1}{2} m_\omega^2 \omega^2 \\
& + \frac{1}{4} c_3 \omega^4 + \frac{1}{2} m_\rho^2 \rho^2 + \Lambda_v \big(g_\omega^2 \omega^2\big)\big(g_\rho^2 \rho^2\big) \\
& + \sum_{l=e,\mu} \frac{1}{3\pi^2} \int_0^{k_F^l} \frac{k^4 dk}{\sqrt{k^2 + m_l^2}},
\end{aligned}
\tag{6}
$$

where $M^* = M + g_\sigma \sigma$ denotes the effective nucleon mass. For hadronic matter in β equilibrium, the chemical potentials satisfy the relations $\mu_p = \mu_n - \mu_e$ and $\mu_\mu = \mu_e$. At zero temperature, the chemical potentials are given by

$$
\mu_i = \sqrt{k_F^i{}^2 + M^{*2}} + g_\omega \omega + g_\rho \tau_3^i \rho, \quad i = p, n, \tag{7}
$$

$$
\mu_l = \sqrt{k_F^l{}^2 + m_l^2}, \qquad\qquad l = e, \mu. \tag{8}
$$

In order to investigate the impact of nuclear symmetry energy on the hadron-quark phase transition, we adopt two successful RMF models, TM1 [42], and IUFSU [43], to describe nuclear interactions. For completeness, we present the parameter sets and saturation properties of these two models in Tables I and II, respectively. It is well known that nuclear symmetry energy $E_{\rm sym}$ and its slope L play a crucial role in determining the properties of neutron stars. To examine the L dependence of hadron-quark pasta phases, we employ two sets of generated models based on the TM1 and IUFSU parametrizations as described in Ref. [66]. We note that all models in each set have the same isoscalar saturation properties and fixed symmetry energy $E_{\rm sym}$ at a density of 0.11 fm^{-3} but have different symmetry energy slope L. It has been reported in Ref. [66] that the choice of fixing symmetry

energy at $n_b = 0.11$ fm^{-3} could produce very similar binding energies of finite nuclei within one set of generated models. The generated models were obtained by simultaneously adjusting g_ρ and Λ_v so as to achieve a given L at saturation density n_0 while keeping $E_{\rm sym}$ fixed at $n_b = 0.11$ fm^{-3}. The parameters, g_ρ and Λ_v, generated from the TM1 and IUFSU models for different L are given in Tables III and IV for completeness. For the TM1 model, we consider that L varies from 50 to 110.8 MeV (original TM1 value). For the IUFSU model, the range of L is from 47.2 (original IUFSU value) to 110 MeV. As one can see in Tables III and IV, there is a positive correlation between the slope parameter L and the symmetry energy at saturation density $E_{\rm sym}(n_0)$. In the case of TM1, we obtain $E_{\rm sym}(n_0) = 32.39$ MeV for $L = 50$ MeV, while $E_{\rm sym}(n_0) = 36.89$ MeV for $L = 110.8$ MeV.

III. QUARK MATTER PHASE

To describe quark matter, we adopt the NJL model with three flavors. The Lagrangian density of the NJL model is given by

$$
\begin{aligned}
\mathcal{L}_{\rm NJL} = & \, \bar{q}(i\gamma_\mu \partial^\mu - m^0) q \\
& + G_S \sum_{a=0}^{8} [(\bar{q}\lambda_a q)^2 + (\bar{q} i\gamma_5 \lambda_a q)^2] \\
& - K\{\det[\bar{q}(1 + \gamma_5)q] + \det[\bar{q}(1 - \gamma_5)q]\} \\
& - G_V \sum_{a=0}^{8} [(\bar{q}\gamma^\mu \lambda_a q)^2 + (\bar{q}\gamma^\mu \gamma_5 \lambda_a q)^2],
\end{aligned}
\tag{9}
$$

where q denotes the quark field with three flavors ($N_f = 3$) and three colors ($N_c = 3$). The current quark mass matrix is given by $m^0 = {\rm diag}(m_u^0, m_d^0, m_s^0)$. We take into account chirally symmetric four-quark interaction with coupling G_S, Kobayashi–Maskawa–'t Hooft (KMT) six-quark interaction with coupling K, and vector interaction with coupling G_V. It has been shown in Refs. [19,20,35–41] that vector interactions in the NJL model play an important role in describing massive stars. In the present work, we use the parameters

TABLE II. Saturation properties of symmetric nuclear matter for the TM1 and IUFSU models. The quantities E_0, K, $E_{\rm sym}$, and L are, respectively, the energy per nucleon, incompressibility coefficient, symmetry energy, and symmetry energy slope at saturation density n_0.

Model	n_0 (fm^{-3})	E_0 (MeV)	K (MeV)	$E_{\rm sym}$ (MeV)	L (MeV)
TM1	0.145	−16.3	281	36.9	110.8
IUFSU	0.155	−16.4	231	31.3	47.2

TABLE III. Parameters g_ρ and Λ_v, generated from the TM1 model for different slope L at saturation density n_0 with fixed symmetry energy $E_{sym} = 28.05$ MeV at a density of 0.11 fm^{-3}. The last line shows the symmetry energy at saturation density n_0. The original TM1 model has $L = 110.8$ MeV.

L (MeV)	50.0	60.0	70.0	80.0	90.0	100.0	110.8
g_ρ	12.2413	11.2610	10.6142	10.1484	9.7933	9.5114	9.2644
Λ_v	0.0327	0.0248	0.0182	0.0128	0.0080	0.0039	0.0000
$E_{sym}(n_0)$ (MeV)	32.39	33.29	34.11	34.86	35.56	36.22	36.89

given in Ref. [71], $m_u^0 = m_d^0 = 5.5$ MeV, $m_s^0 = 140.7$ MeV, $\Lambda = 602.3$ MeV, $G_S \Lambda^2 = 1.835$, and $K\Lambda^5 = 12.36$. The vector coupling G_V is treated as a free parameter following Refs. [19,20,41], since there is still no constraint on G_V at finite density. In Ref. [19], two values were used for the ratio $G_V/G_S = 0.1$ and 0.2. Several values of G_V/G_S between 0 to 0.75 were adopted in Ref. [41]. In the present work we find that, using the TM1 model for the hadronic phase, a pure quark phase does not appear at densities below 20 times the nuclear saturation density for $G_V/G_S > 0.45$, which implies that such a large G_V is not suggested. Therefore, we use $G_V/G_S = 0$ and 0.4 to investigate the effects of vector couplings in the present calculations, where the TM1 model is employed to describe the hadronic phase. Since G_V can only stiffen the EOS of quark matter, the effects of vector couplings on the hadron-quark phase transition using the IUFSU model would be qualitatively similar to the case of using the TM1 model. Furthermore, the onset density of the mixed phase obtained in the IUFSU model is significantly higher than that of the TM1 model (see Fig. 3 below), and therefore we use only $G_V/G_S = 0$ in the calculations with the IUFSU model.

At the mean-field level, the quarks get constituent quark masses by spontaneous chiral symmetry breaking. The constituent quark mass in vacuum m_i is much larger than the current quark mass m_i^0. The constituent quark masses m_i^* in quark matter can be determined by the gap equations

$$m_i^* = m_i^0 - 4G_S\langle \bar{q}_i q_i \rangle + 2K\langle \bar{q}_j q_j \rangle\langle \bar{q}_k q_k \rangle, \quad (10)$$

with (i, j, k) being any permutation of (u, d, s). The energy density of quark matter is given by

$$\varepsilon_{NJL} = \sum_{i=u,d,s}\left[-\frac{3}{\pi^2}\int_{k_F^i}^{\Lambda}\sqrt{k^2 + m_i^{*2}}\,k^2 dk\right]$$
$$+ 2G_S\left(C_u^2 + C_d^2 + C_s^2\right) - 4KC_uC_dC_s$$
$$+ 2G_V\left(n_u^2 + n_d^2 + n_s^2\right) - \varepsilon_0, \quad (11)$$

where $C_i = \langle \bar{q}_i q_i \rangle$ denotes the quark condensate of flavor i. The constant ε_0 is introduced to set $\varepsilon_{NJL} = 0$ in the physical vacuum. In Refs. [29–31], an effective bag constant B^* was introduced since there remains uncertainty in the low-density normalization of pressure in the NJL model. In the present work, our choice of ε_0 corresponds to a vanishing pressure in the vacuum.

The chemical potentials of quarks and leptons in quark matter satisfy the β equilibrium condition, $\mu_s = \mu_d = \mu_u + \mu_e$ and $\mu_\mu = \mu_e$, where the chemical potential of quark flavor i is given by

$$\mu_i = \sqrt{{k_F^i}^2 + m_i^{*2}} + 4G_V n_i. \quad (12)$$

The total energy density and pressure in quark matter are written as

$$\varepsilon_{QP} = \varepsilon_{NJL} + \sum_{l=e,\mu}\frac{1}{\pi^2}\int_0^{k_F^l}\sqrt{k^2 + m_l^2}\,k^2 dk, \quad (13)$$

$$P_{QP} = \sum_{i=u,d,s,e,\mu} n_i\mu_i - \varepsilon_{QP}. \quad (14)$$

IV. HADRON-QUARK MIXED PHASE

In this section, we briefly introduce and compare several methods for the description of hadron-quark mixed phase, namely (1) energy minimization (EM) method, (2) coexisting phases (CP) method, (3) Gibbs construction, and (4) Maxwell construction. We emphasize that the main difference among these methods is the treatment of surface and Coulomb contributions. Generally, the hadron-quark mixed phase can be described by the Wigner-Seitz approximation, where the system is divided into periodically repeating charge-neutral cells. The coexisting hadronic and quark phases inside the cell are separated by a sharp interface where a surface tension often exists. The possible geometric structure of the mixed phase may change from droplet to rod, slab, tube, and bubble with increasing baryon density. In the

TABLE IV. Parameters g_ρ and Λ_v, generated from the IUFSU model for different slope L at saturation density n_0 with fixed symmetry energy $E_{sym} = 26.78$ MeV at a density of 0.11 fm^{-3}. The last line shows the symmetry energy at saturation density n_0. The original IUFSU model has $L = 47.2$ MeV.

L (MeV)	47.2	50.0	60.0	70.0	80.0	90.0	100.0	110.0
g_ρ	13.5900	12.8202	11.1893	10.3150	9.7537	9.3559	9.0558	8.8192
Λ_v	0.0460	0.0420	0.0305	0.0220	0.0153	0.0098	0.0051	0.0011
$E_{sym}(n_0)$ (MeV)	31.30	31.68	32.89	33.94	34.88	35.74	36.53	37.27

EM method, the equilibrium conditions between coexisting hadronic and quark phases are determined by minimization of the total energy including surface and Coulomb contributions, so the finite-size effects due to surface and Coulomb contributions are treated relatively well compared with other methods. In the CP method, the surface and Coulomb energies are perturbatively included, while the Gibbs equilibrium conditions are used for the two coexisting phases. We note that both the Gibbs and Maxwell constructions do not include the finite-size effects. In the Gibbs construction, the surface tension at the hadron-quark interface is assumed to be negligible, hence the surface and Coulomb energies are not taken into account and only global charge neutrality is required. On the other hand, the surface tension in the Maxwell construction is assumed to be extremely large, so that local charge neutrality has to be maintained. The surface tension plays a key role in determining the structure of hadron-quark mixed phase, but its value is poorly known so far. In the present work, we treat the surface tension σ as a free parameter.

In the following subsections, we describe how to determine the equilibrium state of hadron-quark mixed phase at a given baryon density within different methods.

A. Energy minimization method

The Wigner-Seitz approximation is used to describe the hadron-quark mixed phase, where two coexisting phases inside a charge-neutral cell are separated by a sharp interface with a finite surface tension. The leptons (electrons and muons) are assumed to be uniformly distributed throughout the cell. The total energy density of the mixed phase is given by

$$\varepsilon_{\mathrm{MP}} = u\varepsilon_{\mathrm{QP}} + (1-u)\varepsilon_{\mathrm{HP}} + \varepsilon_{\mathrm{surf}} + \varepsilon_{\mathrm{Coul}}, \qquad (15)$$

where $u = V_{\mathrm{QP}}/(V_{\mathrm{QP}} + V_{\mathrm{HP}})$ is the volume fraction of the quark phase. The energy densities, $\varepsilon_{\mathrm{HP}}$ and $\varepsilon_{\mathrm{QP}}$, are given by Eqs. (5) and (13), respectively. The surface and Coulomb energy densities are expressed as

$$\varepsilon_{\mathrm{surf}} = \frac{D\sigma u_{\mathrm{in}}}{r_D}, \qquad (16)$$

$$\varepsilon_{\mathrm{Coul}} = \frac{e^2}{2}(\delta n_c)^2 r_D^2 u_{\mathrm{in}} \Phi(u_{\mathrm{in}}), \qquad (17)$$

with

$$\Phi(u_{\mathrm{in}}) = \begin{cases} \dfrac{1}{D+2}\left(\dfrac{2 - D u_{\mathrm{in}}^{1-2/D}}{D-2} + u_{\mathrm{in}}\right), & D = 1, 3, \\[2ex] \dfrac{u_{\mathrm{in}} - 1 - \ln u_{\mathrm{in}}}{D+2}, & D = 2. \end{cases} \qquad (18)$$

Here, σ denotes the surface tension at the hadron-quark interface, while $D = 1, 2, 3$ is the geometric dimension of the cell with r_D being the size of the inner part. u_{in} represents the volume fraction of the inner part, i.e., $u_{\mathrm{in}} = u$ for droplet, rod, and slab configurations, and $u_{\mathrm{in}} = 1 - u$ for tube and bubble configurations. $e = \sqrt{4\pi/137}$ is the electromagnetic coupling constant. $\delta n_c = n_c^{\mathrm{HP}} - n_c^{\mathrm{QP}}$ is the charge-density difference between hadronic and quark phases. In Eq. (15), the first two terms represent the bulk contributions, while the last two

terms come from the finite-size effects that depend on the size r_D. At a given baryon density, r_D can be determined by minimizing $\varepsilon_{\mathrm{surf}} + \varepsilon_{\mathrm{Coul}}$, which leads to the relation $\varepsilon_{\mathrm{surf}} = 2\varepsilon_{\mathrm{Coul}}$. The size of the inner phase and that of the Wigner-Seitz cell are respectively given by

$$r_D = \left[\frac{\sigma D}{e^2(\delta n_c)^2 \Phi}\right]^{1/3}, \qquad (19)$$

$$r_C = u^{-1/D} r_D. \qquad (20)$$

In the EM method, the equilibrium conditions for coexisting hadronic and quark phases in the Wigner-Seitz cell are derived by minimization of the total energy density (15). At a given baryon density n_b, the energy density of the mixed phase $\varepsilon_{\mathrm{MP}}$ is considered as a function of eight variables: n_p, n_n, n_u, n_d, n_s, n_e, n_μ, and u. The minimization should be performed under the constraints of globe charge neutrality and baryon number conservation, which are expressed as

$$0 = n_e + n_\mu - \frac{u}{3}(2n_u - n_d - n_s) - (1-u)n_p, \quad (21)$$

$$n_b = \frac{u}{3}(n_u + n_d + n_s) + (1-u)(n_p + n_n). \qquad (22)$$

We introduce the Lagrange multipliers, μ_e and μ_n, for the constraints, and then construct a function as

$$w = \varepsilon_{\mathrm{MP}} - \mu_e\left[n_e + n_\mu - \frac{u}{3}(2n_u - n_d - n_s) - (1-u)n_p\right]$$
$$- \mu_n\left[\frac{u}{3}(n_u + n_d + n_s) + (1-u)(n_p + n_n)\right]. \qquad (23)$$

By minimizing w with respect to the particle densities, we obtain the following equilibrium conditions for chemical potentials:

$$\mu_u - \frac{4\varepsilon_{\mathrm{Coul}}}{3u\,\delta n_c} = \frac{1}{3}\mu_n - \frac{2}{3}\mu_e, \qquad (24)$$

$$\mu_d + \frac{2\varepsilon_{\mathrm{Coul}}}{3u\,\delta n_c} = \frac{1}{3}\mu_n + \frac{1}{3}\mu_e, \qquad (25)$$

$$\mu_s + \frac{2\varepsilon_{\mathrm{Coul}}}{3u\,\delta n_c} = \frac{1}{3}\mu_n + \frac{1}{3}\mu_e, \qquad (26)$$

$$\mu_p + \frac{2\varepsilon_{\mathrm{Coul}}}{(1-u)\,\delta n_c} = \mu_n - \mu_e, \qquad (27)$$

$$\mu_\mu = \mu_e. \qquad (28)$$

The equilibrium condition for the pressure at the interface is achieved by minimizing w with respect to the volume fraction u, which can be written as

$$P_{\mathrm{HP}} = P_{\mathrm{QP}} - \frac{2\varepsilon_{\mathrm{Coul}}}{\delta n_c}\left[\frac{1}{3u}(2n_u - n_d - n_s) + \frac{1}{1-u}n_p\right]$$
$$\mp \frac{\varepsilon_{\mathrm{Coul}}}{u_{\mathrm{in}}}\left(3 + u_{\mathrm{in}}\frac{\Phi'}{\Phi}\right), \qquad (29)$$

where the sign of the last term is $-$ for droplet, rod, and slab configurations, while it is $+$ for tube and bubble configurations. The equilibrium equations (24)–(29) are clearly different from the Gibbs equilibrium conditions, which is due to the inclusion of surface and Coulomb energies in the minimization procedure. We define the pressure of the mixed phase

by the thermodynamic relation $P_{MP} = n_b^2 \frac{\partial(\varepsilon_{MP}/n_b)}{\partial n_b}$, which is somewhat different from P_{HP} and P_{QP}. This is similar to the case of nuclear liquid-gas phase transition at subnuclear densities [66–69].

By solving the above equilibrium equations at a given baryon density n_b, we calculate and compare the energy density of the mixed phase with different pasta configurations, and then determine the most stable shape that has the lowest energy density. All thermodynamic quantities of the mixed phase can be computed after the equilibrium state is achieved.

B. Coexisting phases method

In the CP method, the Gibbs equilibrium conditions are used for coexisting hadronic and quark phases. Meanwhile, the surface and Coulomb energies are included perturbatively. This means that the Gibbs equilibrium conditions are derived without the inclusion of surface and Coulomb contributions, but they are taken into account in the total energy density of the mixed phase given by Eq. (15). In fact, we can derive the Gibbs equilibrium conditions by minimizing the total energy density without surface and Coulomb terms. By setting $\varepsilon_{surf} = \varepsilon_{Coul} = 0$ in Eq. (15), we minimize the energy density following the procedure described in the EM method. The resulting equilibrium conditions are given by

$$P_{HP} = P_{QP}, \tag{30}$$

$$\mu_u + \mu_e = \mu_d = \mu_s = \frac{1}{3}\mu_n + \frac{1}{3}\mu_e, \tag{31}$$

$$\mu_p = \mu_n - \mu_e, \tag{32}$$

$$\mu_\mu = \mu_e. \tag{33}$$

which are equivalent to the Gibbs conditions for phase equilibrium in Ref. [11]. After the equilibrium state is achieved by solving Eqs. (30)–(33) at a given baryon density n_b, the energy density of the mixed phase can be calculated from Eq. (15), where the surface and Coulomb energies are taken into account. Compared with the EM method, the CP method can be viewed as a perturbative approximation, in which the surface and Coulomb contributions are regarded as perturbations and their influences on the equilibrium conditions are neglected. Therefore, the EM method is more complete than the CP method, because the surface and Coulomb contributions are included not only in the total energy density of the mixed phase but also in the equilibrium conditions for coexisting phases in the EM method. We emphasize that the shape and size of the mixed phase are determined by competition between surface and Coulomb energies, which are unrelated to the Gibbs conditions. In the CP method, the pressure of the mixed phase satisfies the relation $P_{MP} = P_{HP} = P_{QP}$. This is because the pressure difference between hadronic and quark phases due to the surface tension is neglected in the CP method.

C. Gibbs construction

In the Gibbs construction, the finite-size effects due to surface and Coulomb contributions are neglected completely, so the mixed phase does not include any pasta structures. In this case, the surface tension at the hadron-quark interface

is assumed to be negligible, and global charge neutrality is required. Both hadronic matter and quark matter are allowed to be charged separately. Since only bulk contributions are considered, the energy density of the mixed phase is reduced to

$$\varepsilon_{MP} = u\varepsilon_{QP} + (1 - u)\varepsilon_{HP}, \tag{34}$$

where the surface and Coulomb terms vanish compared with Eq. (15). The equilibrium conditions can be derived from the minimization of Eq. (34), which have been given by Eqs. (30)–(33). The pressure equilibrium between hadronic and quark phases is shown in Eq. (30), while Eq. (31) represents the chemical potential equilibrium between two phases. At a given baryon density n_b, there are two independent chemical potentials, μ_n and μ_e, which can be determined by the constraints of global charge neutrality and baryon number conservation given in Eqs. (21) and (22). The Gibbs equilibrium conditions of Eqs. (30) and (31) imply that coexisting hadronic and quark phases have equal pressures and chemical potentials. After the equilibrium state is determined by Gibbs conditions, all properties of the mixed phase can be calculated.

D. Maxwell construction

In the Maxwell construction, the system satisfies the local charge neutrality condition, namely, both hadronic and quark phases are charge neutral. This is related to an extremely large surface tension at the hadron-quark interface, which disfavors the formation of charged cluster of quark matter immersed in hadronic matter. The energy density of the mixed phase includes only bulk contributions as described in Eq. (34). Due to the local charge neutrality condition, there are three constraints instead of Eqs. (21) and (22), which are expressed as

$$0 = n_c^{HP} = n_e^{HP} + n_\mu^{HP} - n_p, \tag{35}$$

$$0 = n_c^{QP} = n_e^{QP} + n_\mu^{QP} - \frac{1}{3}(2n_u - n_d - n_s), \tag{36}$$

$$n_b = \frac{u}{3}(n_u + n_d + n_s) + (1 - u)(n_p + n_n). \tag{37}$$

In the Maxwell construction, the electron density is usually discontinuous across the interface due to local charge neutrality. We introduce the Lagrange multipliers, μ_e^{HP}, μ_e^{QP}, and μ_n, for these three constraints and construct a function as

$$w = \varepsilon_{MP} - \mu_n\left[\frac{u}{3}(n_u + n_d + n_s) + (1 - u)(n_p + n_n)\right]$$
$$- \mu_e^{QP}u\left[n_e^{QP} + n_\mu^{QP} - \frac{1}{3}(2n_u - n_d - n_s)\right]$$
$$- \mu_e^{HP}(1 - u)\left[n_e^{HP} + n_\mu^{HP} - n_p\right]. \tag{38}$$

By minimizing w with respect to the volume fraction u and particle densities, we obtain the Maxwell conditions for phase equilibrium:

$$P_{HP} = P_{QP}, \tag{39}$$

$$\mu_n = \mu_u + 2\mu_d. \tag{40}$$

Meanwhile, the β equilibrium conditions in hadronic and quark matter are respectively expressed as

$$\mu_p + \mu_e^{\text{HP}} = \mu_n, \tag{41}$$

$$\mu_u + \mu_e^{\text{QP}} = \mu_d = \mu_s. \tag{42}$$

The Maxwell equilibrium conditions mean that coexisting hadronic and quark phases have the same pressure and baryon chemical potential but different electron chemical potential. During the phase transition, the pressure of the mixed phase in the Maxwell construction remains constant. This behavior is different from that in the Gibbs construction, where the pressure of the mixed phase increases with increasing density.

V. RESULTS AND DISCUSSION

In this section, we investigate and compare the pasta structures of hadron-quark mixed phase using the methods described in the previous section. In order to check the model dependence of the results, we use two different RMF models (TM1 and IUFSU) for the description of hadronic matter. Meanwhile, the effects of repulsive vector interactions in the NJL model are also examined. By employing a set of models with different symmetry energy slope L, we discuss the effects of nuclear symmetry energy on the hadron-quark phase transition. The properties of neutron stars are calculated by using the EOS including quark degrees of freedom.

A. Pasta structures in hadron-quark mixed phase

During the hadron-quark phase transition, several pasta configurations may appear in the order of droplet, rod, slab, tube, and bubble with increasing density. It is interesting to check whether all these geometric shapes would occur in the mixed phase and how the pasta phases are affected by the model parameters. To study the pasta structures in hadron-quark mixed phase, we employ the EM and CP methods described in Sec. IV. It is known that the geometric shape and size of the mixed phase are mainly determined by competition between surface and Coulomb energies. Therefore, only the EM and CP methods can be used, whereas the Gibbs and Maxwell constructions cannot describe pasta structures due to the absence of surface and Coulomb contributions. In the EM method, the equilibrium conditions between two coexisting phases are determined by minimizing the total energy including surface and Coulomb contributions. However, in the CP method, the Gibbs equilibrium conditions are adopted that correspond to the balance without finite-size effects, while the surface and Coulomb energies are perturbatively incorporated after the equilibrium state is achieved.

Generally, the energy density difference between two successive configurations is very small compared with the total energy density. In Fig. 1, we compare the energy densities of various pasta phases for $\sigma = 10$ MeV/fm^2 obtained using the EM method relative to those of the Gibbs construction ($\sigma = 0$). The results are calculated with the TM1 parametrization given in Table I, while the vector coupling $G_V = 0$ is adopted in the NJL model. For comparison, the energy densities of pure hadronic and pure quark phases are plotted by black dot-
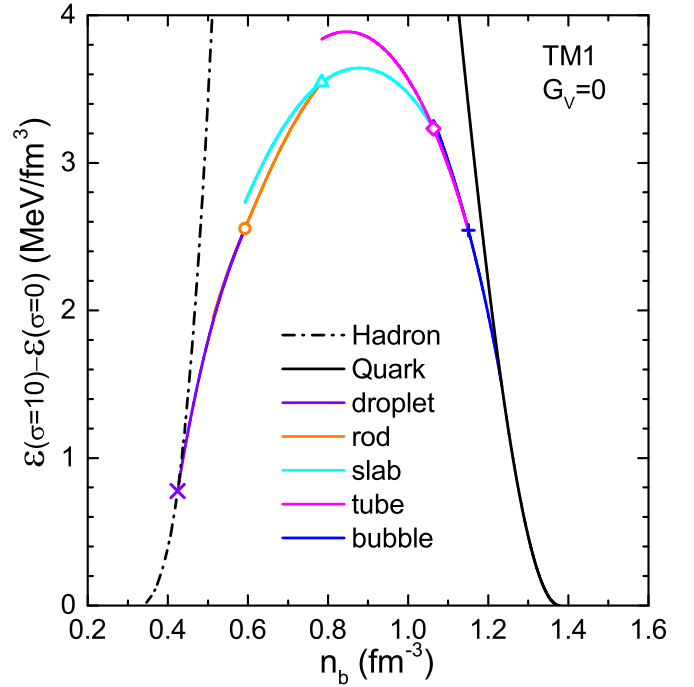

FIG. 1. Comparison of energy densities for various pasta phases obtained using the EM method with $\sigma = 10$ MeV/fm^2 and $G_V = 0$ relative to those of the Gibbs construction ($\sigma = 0$). The filled circles indicate the transition points between different configurations.

dashed and solid lines, respectively. At a given baryon density n_b, the equilibrium state is the one with the lowest energy density. When the energy density of a droplet becomes lower than that of pure hadronic matter, quark droplets are formed in hadronic matter and the hadron-quark phase transition starts. As the density increases, other pasta configurations, such as rod, slab, etc., may appear when each has the lowest energy density among all configurations. The phase transition ends at the point where pure quark matter has lower energy density than pasta phases. It is seen in Fig. 1 that the energy density difference between two successive shapes is rather small, and it is almost invisible between the droplet (bubble) and rod (tube) phases.

To evaluate the difference between the EM and CP methods, we compare in Fig. 2 the energy densities of pasta phases obtained from the two methods with the surface tension $\sigma = 10$ MeV/fm^2, where the transition points between different configurations are indicated by filled circles. In the calculations, the TM1 model is used for hadronic phase, while the NJL model with $G_V = 0$ and $G_V = 0.4\,G_S$ are adopted for quark phase in the left and right panels, respectively. It is shown that the energy densities of the EM method are slightly lower than those of the CP method. This is because there are relatively large configuration space in the EM method, and therefore lower energies could be achieved in the minimization procedure. By comparing the two panels of Fig. 2, one can see that the energy densities for $G_V = 0.4\,G_S$ are significantly larger than those for $G_V = 0$, and the density range of the mixed phase for $G_V = 0.4\,G_S$ is shifted to larger values. This is because repulsive vector interactions in the NJL
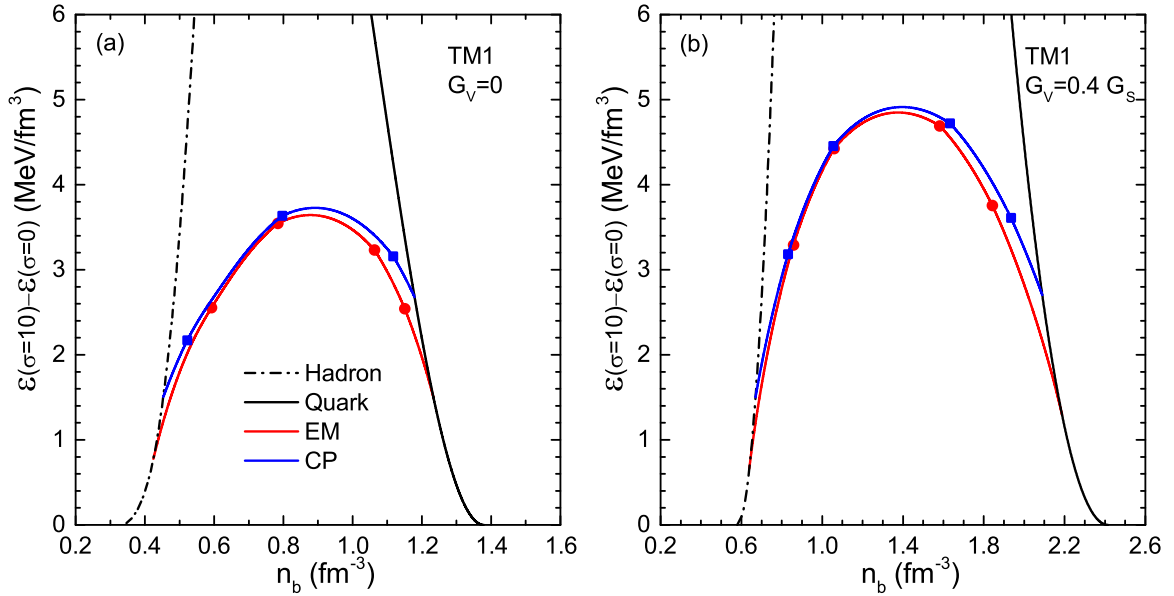
FIG. 2. Comparison of energy densities obtained using the EM and CP methods with $\sigma = 10$ MeV/fm^2, relative to those of the Gibbs construction ($\sigma = 0$). The filled circles (squares) indicate the transition points between different configurations for EM (CP) method.

model can effectively stiffen the EOS of quark matter, which results in a delay of the phase transition.

In order to study how the surface tension σ affects the properties of pasta phases, we present in Fig. 3 the energy densities of the mixed phase obtained using the EM method for several values of σ relative to those of the Gibbs construction ($\sigma = 0$). The filled circles indicate the transition points between different configurations. For comparison, the results obtained in the Maxwell construction are shown by green dotted lines. In the left panel of Fig. 3, the results are obtained by using the TM1 model for hadronic phase and the NJL model with $G_V = 0$ for quark phase. One can see that a larger value of σ leads to a smaller density range and less pasta structures in the mixed phase. With $\sigma = 55$ MeV/fm^2, only droplet, rod, and slab configurations can occur before the system turns to pure quark matter. When the surface tension is larger than the critical value of ≈ 75 MeV/fm^2, the pasta phase is energetically unfavorable because its energy density is higher than that of the Maxwell construction. This means that the Maxwell construction is preferred for such high surface tension. It is

noticeable that no mixed phase would occur inside neutron stars for $\sigma > 75$ MeV/fm^2 because the energetically favored Maxwell construction corresponds to constant pressure. By comparing the left panel ($G_V = 0$) with the middle panel ($G_V = 0.4\,G_S$) in Fig. 3, we see that the repulsive vector interactions in the NJL model can significantly shift the mixed phase toward higher densities with a wider range. This is because the inclusion of repulsive vector interactions increases the energy density of quark matter considerably. Meanwhile, the critical surface tension increases from ≈ 75 MeV/fm^2 for $G_V = 0$ to ≈ 200 MeV/fm^2 for $G_V = 0.4\,G_S$ in the TM1 model. The results of the right panel in Fig. 3 correspond to the case where the IUFSU model is used for hadronic phase and the NJL model with $G_V = 0$ for quark phase. It is found that the mixed phase in the IUFSU model (right panel) is shifted to higher densities with a wider range than that in the TM1 model (left panel), and meanwhile the critical surface tension required by the Maxwell construction rises to ≈ 130 MeV/fm^2 in the IUFSU model from ≈ 75 MeV/fm^2 in the TM1 model. This is mainly because the symmetry
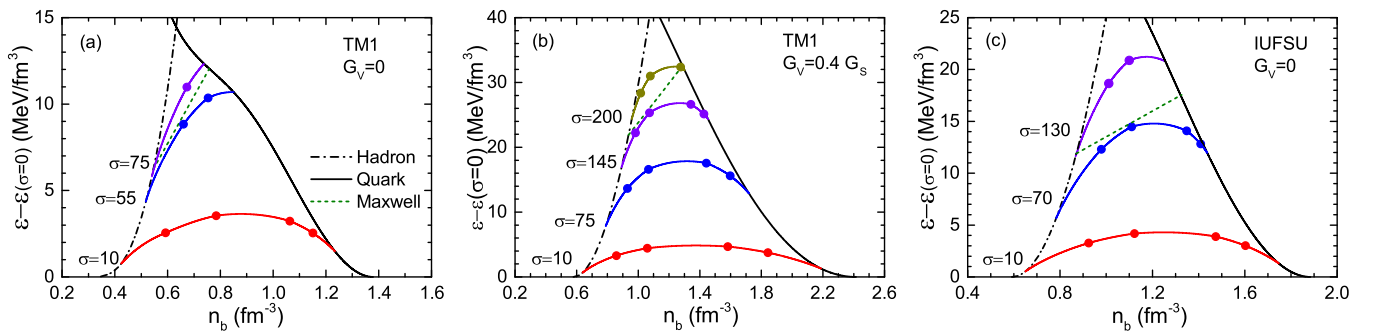

FIG. 3. Energy densities of the mixed phase obtained using the EM method for several values of σ relative to those of the Gibbs construction ($\sigma = 0$). The filled circles indicate the transition points between different configurations. The results of the Maxwell construction are shown by the green dotted lines.
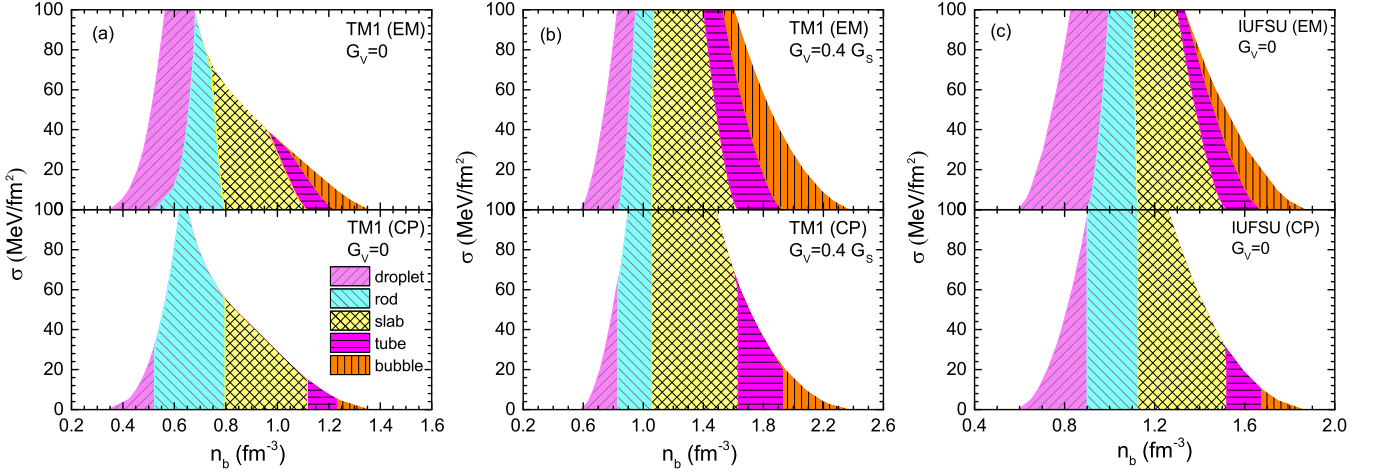
FIG. 4. Density ranges of various pasta shapes as a function of the surface tension σ. The results obtained using the EM and CP methods are displayed in the upper and lower panels, respectively.

energy slope L in the IUFSU model is much smaller than the one in the TM1 model. The effects of the symmetry energy slope L on the pasta phase properties will be discussed in Sec. V B.

In Fig. 4, we show the density ranges of various pasta shapes as a function of the surface tension σ. The results obtained from the EM and CP methods are displayed in the upper and lower panels, respectively. We can see that the onsets of all pasta shapes in the CP method are independent of σ. This is because the equilibrium state in the CP method is determined by the Gibbs conditions, which are unrelated to the surface tension σ. At a given baryon density n_b, the favorable pasta shape is determined by the sum of $\varepsilon_{\mathrm{surf}} + \varepsilon_{\mathrm{Coul}}$, which is proportional to $\sigma^{2/3}$ derived from Eqs. (16)–(20). The transition between two pasta shapes occurs at the density where their energy difference changes sign. Therefore, the transition density in the CP method cannot be influenced by the surface tension σ due to the simple dependence $\varepsilon_{\mathrm{surf}} +$

$\varepsilon_{\mathrm{Coul}} \propto \sigma^{2/3}$. However, the dependence of $\varepsilon_{\mathrm{surf}} + \varepsilon_{\mathrm{Coul}}$ on the surface tension σ is much more complicated in the EM method, since the finite-size effects have been included in the equilibrium conditions. Therefore, the transition density obtained in the EM method is clearly dependent on σ as shown in the upper panels of Fig. 4. As σ increases, the density range of hadron-quark mixed phase significantly shrinks and the number of pasta configurations is reduced. As shown in the upper-left panel of Fig. 4, the pasta phases can be formed even if the surface tension is larger than the critical value of ≈ 75 MeV/fm^2 required by the Maxwell construction. However, the mixed phase for $\sigma > 75$ MeV/fm^2 would not occur in neutron stars, because the energetically favored Maxwell construction corresponds to constant pressure. It is found that the qualitative behaviors of pasta structures are very similar in all panels of Fig. 4, although there are quantitative differences. In the present work, we focus on the study of pasta structures in hadron-quark mixed phase, so a relatively
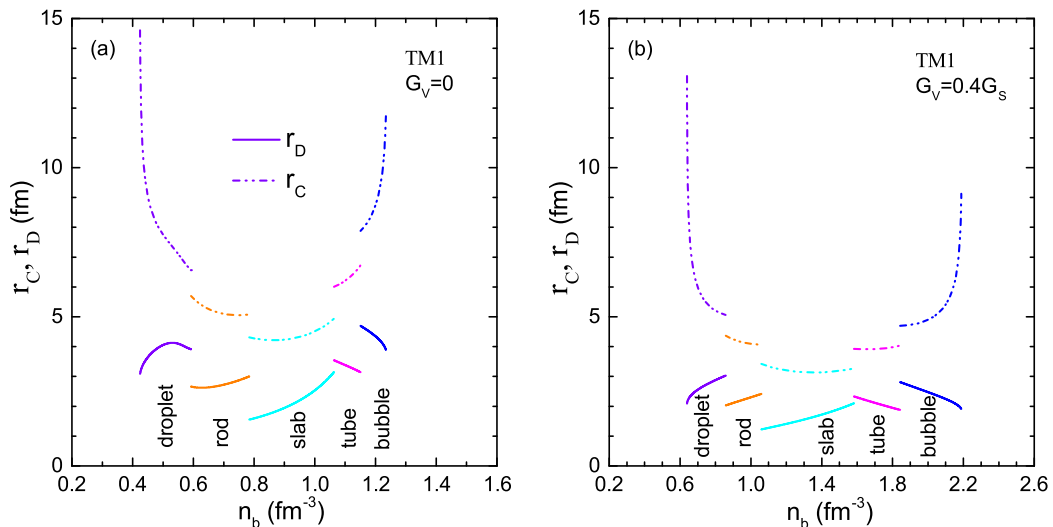

FIG. 5. Size of the Wigner-Seitz cell (r_C) and that of the inner part (r_D) as a function of n_b obtained using the EM method with $\sigma = 10$ MeV/fm^2.
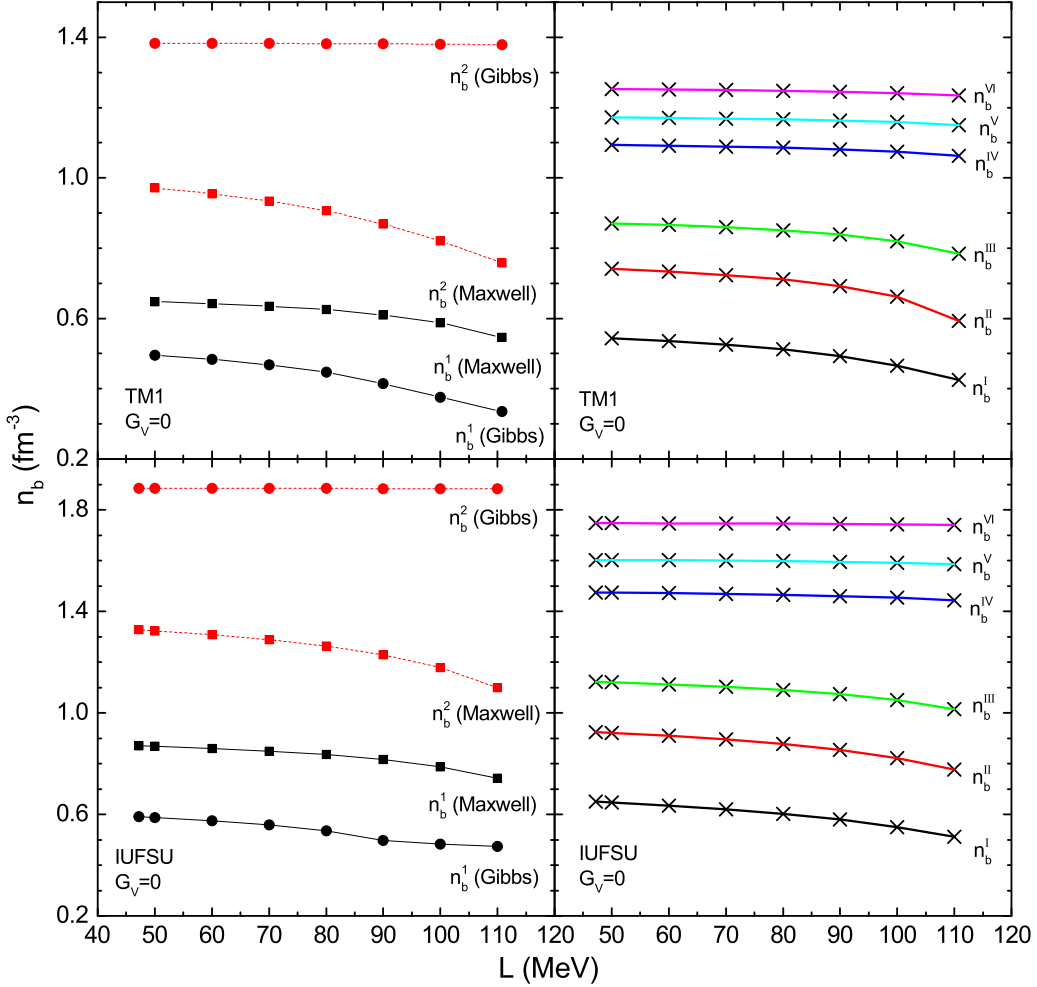
FIG. 6. Transition densities as a function of the symmetry energy slope L. The right panels show results obtained using the EM method with $\sigma = 10$ MeV/fm^2, where onset densities are in the order of n_b^{I} (droplet), n_b^{II} (rod), n_b^{III} (slab), n_b^{IV} (tube), n_b^{V} (bubble), and n_b^{VI} (pure quark matter). The left panels present starting densities (n_b^1) and ending densities (n_b^2) of the mixed phase obtained with the Gibbs and Maxwell constructions.

small surface tension ($\sigma = 10$ MeV/fm^2) will be used in the following calculations.

In Fig. 5, the size of the Wigner-Seitz cell (r_C) and that of the inner part (r_D) obtained using the EM method in the TM1 model are displayed as a function of the baryon density n_b. The results with $G_V = 0$ and $G_V = 0.4 \, G_S$ are presented in the left and right panels, respectively. It is found that there are obvious discontinuities in r_D and r_C at the transition points between different shapes. One can see that r_C decreases rapidly at lower densities, while it increases significantly in the bubble phase before turning to pure quark matter. This behavior is related to a monotonic increase of the volume fraction of quark phase, u, during the phase transition. The tendency for $G_V = 0.4 \, G_S$ (right panel) is similar to that for $G_V = 0$ (left panel), but the density range is shifted to larger values.

B. Symmetry energy effects

To study the effects of nuclear symmetry energy on the hadron-quark phase transition, we use two sets of generated RMF models based on the TM1 and IUFSU parametrizations

as described in Ref. [66]. We emphasize that all models in each set have the same isoscalar saturation properties and fixed symmetry energy E_{sym} at a density of 0.11 fm^{-3} but have different symmetry energy slope L. Therefore, these models could predict very similar properties of finite nuclei but different density dependence of nuclear symmetry energy, which plays an important role in understanding the structure of neutron stars. In Fig. 6, we present the transition densities as a function of the symmetry energy slope L in the TM1 (upper panels) and IUFSU (lower panels) sets. The results are obtained with $G_V = 0$ and $\sigma = 10$ MeV/fm^2. In the right panels, we display the onset densities of droplet (n_b^{I}), rod (n_b^{II}), slab (n_b^{III}), tube (n_b^{IV}), bubble (n_b^{V}), and pure quark matter (n_b^{VI}) obtained using the EM method. In the left panels, we show starting densities (n_b^1) and ending densities (n_b^2) of the mixed phase obtained with the Gibbs and Maxwell constructions. Detailed results are also presented in Table V. One can see that as L increases, all transition densities decrease and the L dependence becomes weaker at the end of the mixed phase. This is because the fraction of hadronic matter monotonically decreases during the hadron-quark phase transition, and

TABLE V. Onset densities of various phases obtained in the TM1 and IUFSU sets. In the EM method, the surface tension $\sigma = 10$ MeV/fm^2 is used and onset densities are in the order of $n_b^{\rm I}$ (droplet), $n_b^{\rm II}$ (rod), $n_b^{\rm III}$ (slab), $n_b^{\rm IV}$ (tube), $n_b^{\rm V}$ (bubble), and $n_b^{\rm VI}$ (pure quark matter). In the Gibbs and Maxwell constructions, n_b^1 and n_b^2 denote the starting and ending densities of the mixed phase, respectively. All densities are in fm^{-3}.

Model		Gibbs		Maxwell		EM					
	L (MeV)	n_b^1	n_b^2	n_b^1	n_b^2	$n_b^{\rm I}$	$n_b^{\rm II}$	$n_b^{\rm III}$	$n_b^{\rm IV}$	$n_b^{\rm V}$	$n_b^{\rm VI}$
TM1	50	0.4957	1.3832	0.64774	0.97204	0.5438	0.7407	0.8708	1.0934	1.1720	1.2529
$G_V = 0$	60	0.4842	1.3828	0.64244	0.95529	0.5358	0.7333	0.8659	1.0915	1.1706	1.2516
	70	0.4683	1.3825	0.63520	0.93349	0.5254	0.7236	0.8595	1.0891	1.1688	1.2500
	80	0.4473	1.3820	0.62537	0.90600	0.5122	0.7109	0.8511	1.0861	1.1666	1.2479
	90	0.4150	1.3813	0.61029	0.86855	0.4931	0.6918	0.8386	1.0816	1.1634	1.2451
	100	0.3751	1.3803	0.58716	0.82095	0.4655	0.6626	0.8198	1.0751	1.1588	1.2410
	110.8	0.3351	1.3786	0.54633	0.75782	0.4246	0.5924	0.7844	1.0632	1.1505	1.2340
lTM1 $G_V = 0.4 \, G_S$	110.8	0.5791	2.4156	0.93703	1.28827	0.6392	0.8577	1.0586	1.5825	1.8428	2.1879
IUFSU	47.2	0.5914	1.8842	0.87046	1.32709	0.6499	0.9241	1.1218	1.4741	1.6025	1.7472
$G_V = 0$	50	0.5880	1.8842	0.86836	1.32319	0.6468	0.9212	1.1199	1.4735	1.6022	1.7471
	60	0.5745	1.8841	0.85985	1.30751	0.6345	0.9097	1.1121	1.4712	1.6010	1.7466
	70	0.5579	1.8840	0.84920	1.28817	0.6199	0.8958	1.1025	1.4684	1.5995	1.7460
	80	0.5351	1.8838	0.83518	1.26304	0.6020	0.8781	1.0902	1.4649	1.5976	1.7452
	90	0.4972	1.8836	0.81574	1.22869	0.5795	0.8547	1.0738	1.4601	1.5952	1.7442
	100	0.4835	1.8833	0.78682	1.17803	0.5502	0.8221	1.0500	1.4532	1.5916	1.7428
	110	0.4733	1.8829	0.74264	1.09978	0.5111	0.7763	1.0144	1.4425	1.5916	1.7407

therefore the influence of nuclear symmetry energy gets weaker and weaker. It is shown that the onset densities of pure quark matter, $n_b^{\rm VI}$ (right panels) and n_b^2 of Gibbs (left panels), are almost independent of L.

In order to understand the L dependence of the transition densities, we show in Fig. 7 the pressure P as a function of the neutron chemical potential μ_n for different values of L in the TM1 (left panel) and IUFSU (right panel) sets. According to the Maxwell equilibrium conditions given by Eqs. (39) and (40), the phase transition occurs at the crossing of the hadronic EOS with the quark EOS, where two phases have the

same pressure and neutron chemical potential. In the hadronic phase, a smaller L corresponds to a larger P, which leads to a larger value of μ_n in the mixed phase with the Maxwell constructions. Therefore, the transition densities for a small L would be higher than those for a large L.

It is interesting to look at the behavior of the electron chemical potential μ_e and its L dependence. Generally, μ_e is considered as a signal of the imbalance between protons and neutrons in hadronic matter under β equilibrium due to the relation $\mu_e = \mu_n - \mu_p$, which is closely related to nuclear symmetry energy $E_{\rm sym}$. Therefore, a larger μ_e implies that the
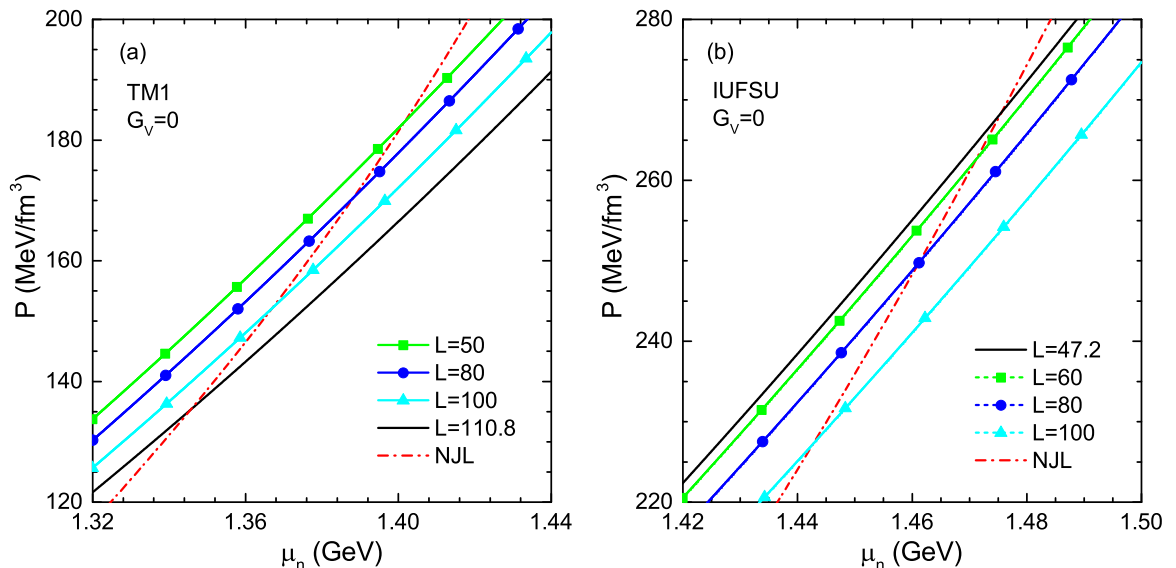

FIG. 7. Pressure P as a function of the neutron chemical potential μ_n for different values of L.
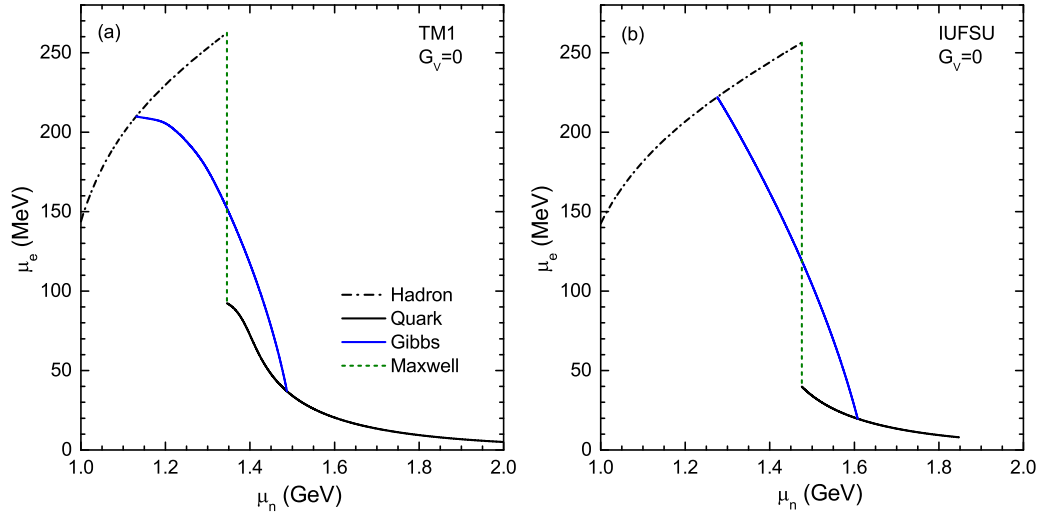
FIG. 8. Electron chemical potential μ_e as a function of the neutron chemical potential μ_n obtained with the Gibbs and Maxwell constructions.

system is more asymmetric. In Fig. 8, we show the electron chemical potential μ_e as a function of the neutron chemical potential μ_n obtained with the Gibbs and Maxwell constructions. The results of the original TM1 ($L = 110.8$ MeV) and IUFSU ($L = 47.2$ MeV) models are presented in the left and right panels, respectively. $G_V = 0$ is adopted in the NJL model. It is seen that μ_e at the transition point with the

Maxwell construction is discontinuous, where μ_e of hadronic phase is much larger than that of quark phase. By comparing the two panels of Fig. 8, we can see that μ_e of TM1 in pure hadronic matter is steeper than that of IUFSU. This is because the symmetry energy slope L of TM1 is much larger than that of IUFSU. As a result, the TM1 model predicts larger μ_e and smaller μ_n for the hadron-quark phase transition with the
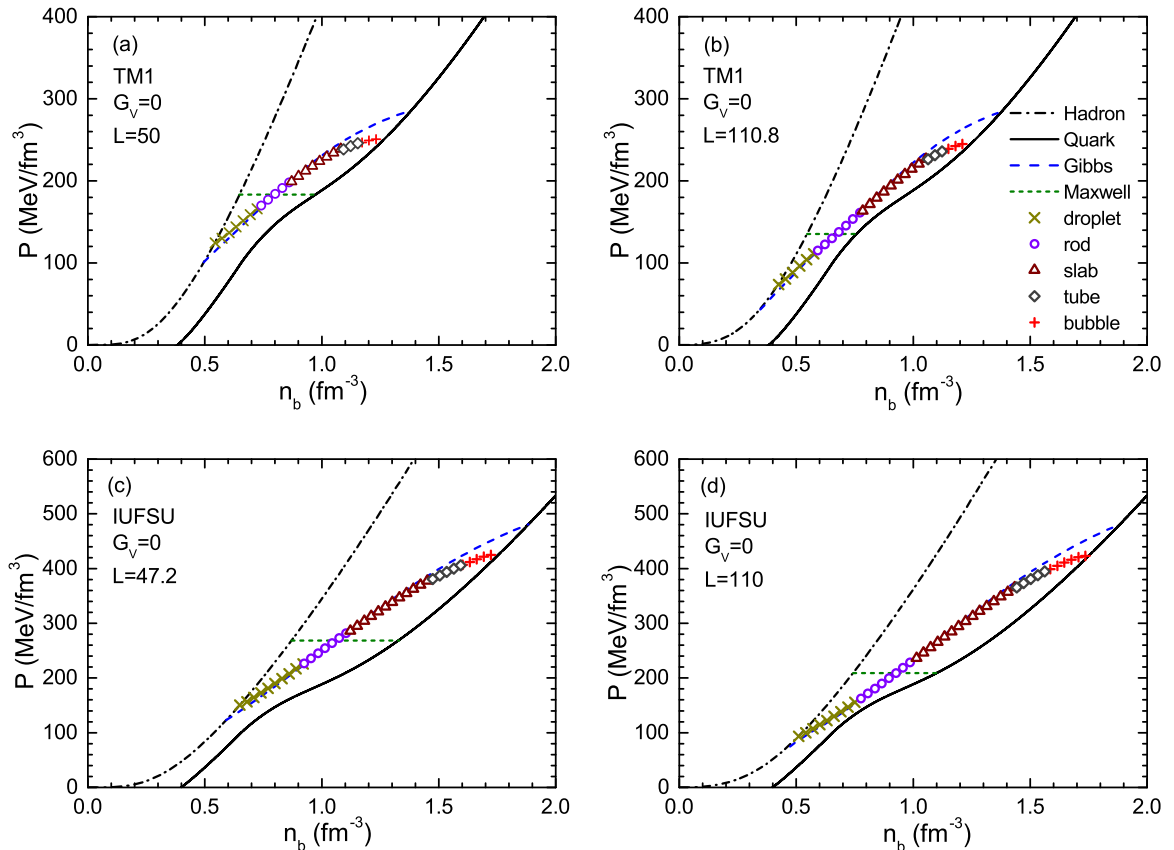

FIG. 9. Pressures as a function of the baryon density for hadronic, mixed, and quark phases. The results of pasta phases obtained using the EM method with $\sigma = 10$ MeV/fm^2 are compared to those of the Gibbs and Maxwell constructions.
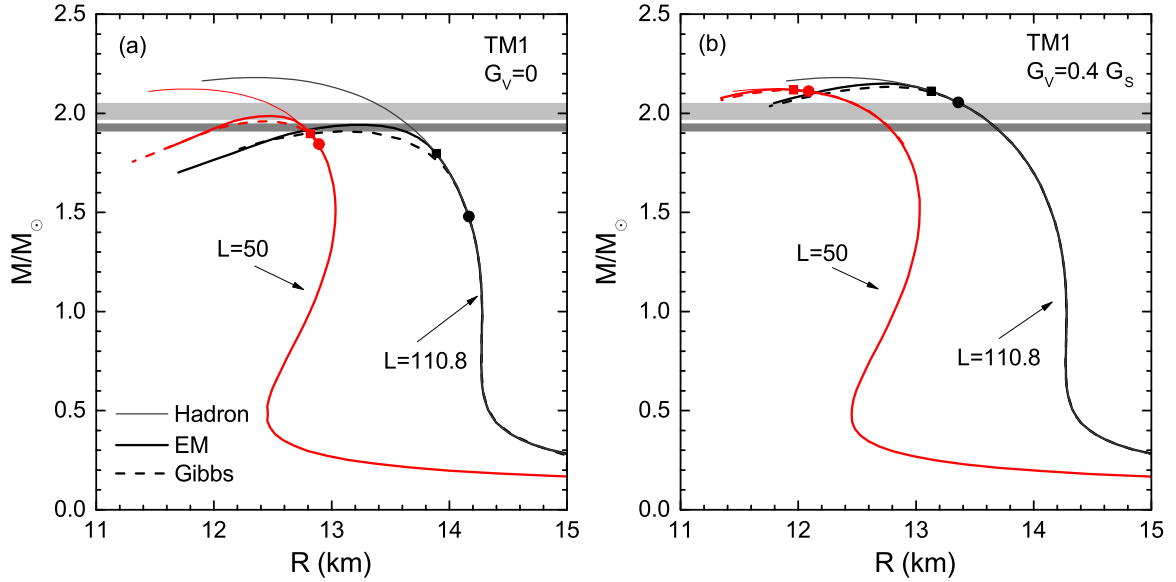
FIG. 10. Mass-radius relations of neutron stars for different EOS. The surface tension $\sigma = 10\,\text{MeV/fm}^2$ is used in the EM method. For comparison, results obtained using pure hadronic EOS are shown by thin solid lines. The filled squares and circles indicate the onset of the star containing a hadron-quark mixed phase within the EM method and Gibbs construction, respectively. The lighter and darker shaded regions correspond to the observational constraints of PSR J0348–0432 ($M = 2.01 \pm 0.04\,M_\odot$) [74] and PSR J1614–2230 ($M = 1.928 \pm 0.017\,M_\odot$) [72,73], respectively.

Maxwell construction. We note that the pressure and chemical potentials remain constant during the phase transition with the Maxwell construction. However, for the Gibbs construction, μ_e and μ_n in the mixed phase can extend over a finite range, and there is no abrupt jump in μ_e between coexisting hadronic and quark phases. The behaviors of μ_e and μ_n obtained using the CP method should be the same as those of the Gibbs construction, since the Gibbs conditions are used to determine the equilibrium state in the CP method.

C. Properties of neutron stars

In Fig. 9, we show the pressures as a function of the baryon density for hadronic, mixed, and quark phases. The results with $L = 50$ MeV and $L = 110.8$ MeV in the TM1 set are displayed in the upper panels, while those with $L = 47.2$ MeV and $L = 110$ MeV in the IUFSU set are shown in the lower panels. In the calculations, the parameters $G_V = 0$ and $\sigma = 10\,\text{MeV/fm}^2$ are used. The pressures of pasta phases are obtained using the EM method, while those with the Gibbs and Maxwell constructions are shown for comparison. It is clearly seen that the pressures of pasta phases are very close to those of the Gibbs construction, while the pressures of the Maxwell construction are constant shown by the green dotted lines. The effects of symmetry energy slope L on the EOS can be observed by comparing the left and right panels. It is shown that a smaller L results in relatively larger pressures and higher onset densities of the mixed phase. We find that qualitative behaviors of the EOS are very similar between the TM1 and IUFSU sets, although quantitative differences exist.

The properties of neutron stars can be obtained by solving the Tolman-Oppenheimer-Volkoff (TOV) equation using the EOS described above, which is matched to the low-density EOS constructed from the Thomas-Fermi ap-

proximation within the TM1 model for the description of neutron-star crusts [44]. In Fig. 10, we display the mass-radius relations obtained in the TM1 set with $L = 50$ MeV and $L = 110.8$ MeV, where the observational constraints of PSR J1614–2230 ($M = 1.928 \pm 0.017\,M_\odot$) [72,73] and PSR J0348 + 0432 ($M = 2.01 \pm 0.04\,M_\odot$) [74] are shown by the darker and lighter shaded regions, respectively. The results with $G_V = 0$ and $G_V = 0.4\,G_S$ are presented in the left and right panels, respectively. For comparison, results obtained using pure hadronic EOS are shown by thin solid lines. It is observed that including quark degrees of freedom can soften the EOS and reduce the maximum mass of neutron stars. The star masses obtained using the EM method are slightly larger than those of the Gibbs construction due to finite-size effects. The influence of symmetry energy slope L is obvious, especially on the radius of neutron stars. By comparing the left and right panels, we find that repulsive vector interactions in the NJL model can significantly increase the maximum mass of neutron stars. To analyze neutron-star properties in more detail, we present in Table VI the structural properties of neutron stars with the maximum mass in several cases. It is seen that, in most cases, deconfined quarks can exist in the core of massive stars either in mixed phase or in pure quark phase. We emphasize that the mixed phase with the Maxwell construction is not allowed to occur in neutron stars due to its constant pressure, but it is still possible to form small size of pure quark matter in special cases (see Table VI) when the surface tension is as high as required by the Maxwell construction. On the other hand, the mixed phase with the Gibbs construction is likely present in the interior of neutron stars, whose size depends on the vector coupling G_V. The results obtained using the EM method indicate that hadron-quark pasta phases may occur in the core of massive

TABLE VI. Properties of neutron stars with the maximum mass M_{max}. The central baryon number density is denoted by n_c, while R_{QP}, R_{MP}, and R correspond to radii of pure quark phase, mixed phase, and whole star, respectively. The surface tension $\sigma = 10$ MeV/fm^2 is used in the EM method.

Model	L (MeV)	Method	M_{max} ($M_{\odot}$)	n_c (fm^{-3})	R_{QP} (km)	R_{MP} (km)	R (km)
TM1	$L = 50$	Gibbs	1.96	0.80		5.10	12.41
$G_V = 0$		EM	1.98	0.80		4.08	12.44
		Maxwell	2.04	0.65	0.25		12.46
	$L = 110.8$	Gibbs	1.91	0.76		7.80	13.09
		EM	1.94	0.70		5.60	13.30
		Maxwell	2.04	0.77	0.82		13.40
TM1	$L = 50$	Gibbs	2.12	0.87		2.31	11.97
$G_V = 0.4\,G_S$		EM	2.12	0.92		1.71	11.84
	$L = 110.8$	Gibbs	2.13	0.80		4.50	12.77
		EM	2.15	0.79		3.41	12.77
IUFSU	$L = 47.2$	Gibbs	1.84	0.91		4.71	11.64
$G_V = 0$		EM	1.86	0.91		3.91	11.67
	$L = 110$	Gibbs	1.80	0.89		6.00	12.30
		EM	1.83	0.82		5.11	12.48

stars, which yield relatively larger M_{max} and smaller R_{MP} than those of the Gibbs construction due to finite-size effects. It is unlikely to form pure quark matter in neutron stars both with the Gibbs construction and in the EM method, since the central density n_c in these cases is lower than the onset of pure quark matter. By comparing results with different values of L, we can see that neutron-star structures are significantly dependent on the symmetry energy slope L.

VI. CONCLUSIONS

In this work, we studied the properties of hadron-quark mixed phase, which may occur in the interior of massive neutron stars. The RMF model was used to describe the hadronic phase, while the NJL model was adopted for the quark phase. We employed the Wigner-Seitz approximation to describe the hadron-quark mixed phase, where coexisting hadronic and quark phases are separated by a sharp interface. We performed the calculations for pasta phases within the EM method, where the equilibrium state at a given baryon density could be determined by minimization of the total energy including surface and Coulomb contributions. The equilibrium conditions derived in the EM method are somewhat different from the Gibbs conditions due to finite-size effects. A simple CP method was also used and compared for the description of hadron-quark pasta phases, where two coexisting phases satisfy Gibbs conditions for phase equilibrium, while the surface and Coulomb energies are perturbatively included after the equilibrium state is achieved. It was found that pasta structures depend on the surface tension σ, and a smaller value of σ could lead to more pasta configurations during the hadron-quark phase transition. Comparing with the results by the EM method, fewer pasta configurations would be present and the transition density between different shapes is independent of σ in the CP method. We have compared the properties of hadron-quark mixed phase obtained from the EM and CP methods with those from the Gibbs and Maxwell

constructions, which include only bulk contributions without finite-size effects. Since the Gibbs and Maxwell constructions correspond respectively to the two limits of zero and very large surface tension, results of the EM and CP methods with finite σ were found to lie between those of the Gibbs and Maxwell constructions.

To investigate the effects of nuclear symmetry energy on the hadron-quark phase transition, we employed two successful RMF models (TM1 and IUFSU), which could provide good descriptions of finite nuclei and acceptable maximum mass of neutron stars. It was found that the IUFSU model predicted higher onset and wider range of the mixed phase compared with the TM1 model. The qualitative behaviors are similar between these two models. In order to examine the influence of symmetry energy slope L, we adopted two sets of generated models based on the TM1 and IUFSU parametrizations. All models in each set have the same isoscalar saturation properties and fixed symmetry energy at the density $n_b = 0.11$ fm^{-3} but have different symmetry energy slope L. It has been shown that as L increases, the transition densities between different pasta configurations decrease slightly, and this tendency becomes weaker at the end of the mixed phase. This means that the starting density of the mixed phase is more sensitive to the value of L, compared with the ending density. The influences of repulsive vector interactions in the NJL model have been evaluated by comparing results of $G_V = 0$ and $G_V = 0.4\,G_S$. The inclusion of repulsive vector interactions could significantly increase the quark matter energy density and stiffen the EOS of quark matter. This trend becomes more apparent with increasing density. As a result, the mixed phase with $G_V = 0.4\,G_S$ would be shifted toward higher densities with a wider range, compared to the case of $G_V = 0$. Meanwhile, the critical densities of various pasta phases are also dependent on the vector coupling G_V.

We calculated properties of neutron stars by using the EOS with quark degrees of freedom. The inclusion of hadron-quark mixed phase could considerably soften the EOS and reduce

the maximum mass of neutron stars. The star masses obtained using the EM method are slightly larger than those of the Gibbs construction due to finite-size effects, but lower than those of the Maxwell construction and pure hadronic matter. The neutron-star radius is closely related to the symmetry energy slope L. The repulsive vector interactions in the NJL model could significantly increase the maximum mass of neutron stars. Generally, there is a critical surface tension above which the energy density of the mixed phase in the EM method is higher than the one in the Maxwell construction, and, as a result, no mixed phase would occur inside neutron stars because the energetically favored Maxwell construction corresponds to constant pressure. It was found that the critical surface tension obtained using the TM1 model is about 75 MeV/fm^2 for $G_V = 0$ adopted in the NJL model, while it

increases to ≈ 200 MeV/fm^2 for $G_V = 0.4\, G_S$. When a small surface tension like $\sigma = 10$ MeV/fm^2 was used, we found that in most cases hadron-quark pasta phases could occur in the core of massive stars, but it is unlikely to form pure quark matter. The resulting maximum masses of neutron stars are almost compatible with the observations of PSR J1614–2230 and PSR J0348 + 0432. We emphasize that both nuclear symmetry energy and repulsive vector interactions in the NJL model can affect structural properties of neutron stars.

[1] H. Heiselberg and M. Hjorth-Jensen, Phys. Rep. **328**, 237 (2000).

[2] N. K. Glendenning, Phys. Rep. **342**, 393 (2001).

[3] F. Weber, Prog. Part. Nucl. Phys. **54**, 193 (2005).

[4] N. K. Glendenning, Phys. Rev. D **46**, 1274 (1992).

[5] K. Schertler, S. Leupold, and J. Schaffner-Bielich, Phys. Rev. C **60**, 025801 (1999).

[6] K. Schertler, C. Greiner, J. Schaffner-Bielich, and M. H. Thoma, Nucl. Phys. A **677**, 463 (2000).

[7] A. W. Steiner, M. Prakash, and J. M. Lattimer, Phys. Lett. B **486**, 239 (2000).

[8] G. F. Burgio, M. Baldo, P. K. Sahu, and H.-J. Schulze, Phys. Rev. C **66**, 025802 (2002).

[9] D. P. Menezes and C. Providência, Phys. Rev. C **68**, 035804 (2003).

[10] B. K. Sharma, P. K. Panda, and S. K. Patra, Phys. Rev. C **75**, 035808 (2007).

[11] F. Yang and H. Shen, Phys. Rev. C **77**, 025801 (2008).

[12] J. Xu, L. W. Chen, C. M. Ko, and B. A. Li, Phys. Rev. C **81**, 055803 (2010).

[13] H. Chen, G. F. Burgio, H.-J. Schulze, and N. Yasutake, Astron. Astrophys. **551**, A13 (2013).

[14] M. Orsaria, H. Rodrigues, F. Weber, and G. A. Contrera, Phys. Rev. C **89**, 015806 (2014).

[15] A. Bhattacharyya, I. N. Mishustin, and W. Greiner, J. Phys. G **37**, 025201 (2010).

[16] H. Heiselberg, C. J. Pethick, and E. F. Staubo, Phys. Rev. Lett. **70**, 1355 (1993).

[17] T. Endo, T. Maruyama, S. Chiba, and T. Tatsumi, Prog. Theor. Phys. **115**, 337 (2006).

[18] T. Maruyama, S. Chiba, H.-J. Schulze, and T. Tatsumi, Phys. Rev. D **76**, 123015 (2007).

[19] N. Yasutake, R. Łastowiecki, S. Benić, D. Blaschke, T. Maruyama, and T. Tatsumi, Phys. Rev. C **89**, 065803 (2014).

[20] W. M. Spinella, F. Weber, G. A. Contrera, and M. G. Orsaria, Eur. Phys. J. A **52**, 61 (2016).

[21] X. H. Wu and H. Shen, Phys. Rev. C **96**, 025802 (2017).

[22] M. S. Berger and R. L. Jaffe, Phys. Rev. C **35**, 213 (1987); **44**, 566 (1991).

[23] G. Lugones and A. G. Grunfeld, Phys. Rev. C **95**, 015804 (2017).

[24] G. Lugones and A. G. Grunfeld, Phys. Rev. C **99**, 035804 (2019).

[25] G. Lugones, A. G. Grunfeld, and M. A. Ajmi, Phys. Rev. C **88**, 045803 (2013).

[26] M. B. Pinto, V. Koch, and J. Randrup, Phys. Rev. C **86**, 025203 (2012).

[27] T. Hatsuda and T. Kunihiro, Phys. Rep. **247**, 221 (1994).

[28] M. Buballa, Phys. Rep. **407**, 205 (2005).

[29] C. H. Lenzi and G. Lugones, Astrophys. J. **759**, 57 (2012)

[30] D. Logoteta, C. Providência, and I. Vidaña, Phys. Rev. C **88**, 055802 (2013).

[31] L. Bonanno and A. Sedrakian, Astron. Astrophys. **539**, A16 (2012).

[32] K. Fukushima, Phys. Rev. D **77**, 114028 (2008); **78**, 039902(E) (2008).

[33] H. Ueda, T. Z. Nakano, A. Ohnishi, M. Ruggieri, and K. Sumiyoshi, Phys. Rev. D **88**, 074006 (2013).

[34] M. Buballa and S. Carignano, Prog. Part. Nucl. Phys. **81**, 39 (2015).

[35] G. Pagliara and J. Schaffner-Bielich, Phys. Rev. D **77**, 063004 (2008).

[36] H. Abuki, R. Gatto, and M. Ruggieri, Phys. Rev. D **80**, 074019 (2009).

[37] K. Masuda, T. Hatsuda, and T. Takatsuka, Astrophys. J. **764**, 12 (2013); Prog. Theor. Exp. Phys. **2013**, 073D01 (2013).

[38] D. P. Menezes, M. B. Pinto, L. B. Castro, P. Costa, and C. Providência, Phys. Rev. C **89**, 055207 (2014).

[39] T. Hell and W. Weise, Phys. Rev. C **90**, 045801 (2014).

[40] P. C. Chu, X. Wang, L. W. Chen, and M. Huang, Phys. Rev. D **91**, 023003 (2015).

[41] R. C. Pereira, P. Costa, and C. Providência, Phys. Rev. D **94**, 094001 (2016).

[42] Y. Sugahara and H. Toki, Nucl. Phys. A **579**, 557 (1994).

[43] F. J. Fattoyev, C. J. Horowitz, J. Piekarewicz, and G. Shen, Phys. Rev. C **82**, 055803 (2010).

[44] H. Shen, Phys. Rev. C **65**, 035802 (2002).

[45] H. Shen, H. Toki, K. Oyamatsu, and K. Sumiyoshi, Astrophys. J. Suppl. **197**, 20 (2011).

[46] J. Carriere, C. J. Horowitz, and J. Piekarewicz, Astrophys. J. **593**, 463 (2003).

[47] R. Cavagnoli, D. P. Menezes, and C. Providência, Phys. Rev. C **84**, 065810 (2011).

[48] S. S. Bao and H. Shen, Phys. Rev. C **89**, 045807 (2014).

[49] S. S. Bao and H. Shen, Phys. Rev. C **91**, 015807 (2015).

[50] C. Providência and A. Rabhi, Phys. Rev. C **87**, 055801 (2013).

[51] B. A. Li, L. W. Chen, and C. M. Ko, Phys. Rep. **464**, 113 (2008).

[52] C. J. Horowitz and J. Piekarewicz, Phys. Rev. Lett. **86**, 5647 (2001).

[53] K. Oyamatsu and K. Iida, Phys. Rev. C **75**, 015801 (2007).

[54] C. Ducoin, J. Margueron, and C. Providência, Europhys. Lett. **91**, 32001 (2010).

[55] Z. Zhang and L. W. Chen, Phys. Lett. B **726**, 234 (2013).

[56] M. Baldo and G. F. Burgio, Prog. Part. Nucl. Phys. **91**, 203 (2016).

[57] M. Oertel, M. Hempel, T. Klähn, and S. Typel, Rev. Mod. Phys. **89**, 015007 (2017).

[58] I. Tews, J. M. Lattimer, A. Ohnishi, and E. E. Kolomeitsev, Astrophys. J. **848**, 105 (2017).

[59] K. Hebeler, J. M. Lattimer, C. J. Pethick, and A. Schwenk, Astrophys. J. **773**, 11 (2013).

[60] J. M. Lattimer and A. W. Steiner, Eur. Phys. J. A **50**, 40 (2014).

[61] G. Hagen, A. Ekström, C. Forssén, G. R. Jansen, W. Nazarewicz, T. Papenbrock, K. A. Wendt, S. Bacca, N. Barnea, B. Carlsson, C. Drischler, K. Hebeler, M. Hjorth-Jensen, M. Miorelli, G. Orlandini, A. Schwenk, and J. Simonis, Nat. Phys. **12**, 186 (2015)

[62] P. Danielewicz and J. Lee, Nucl. Phys. A **922**, 1 (2014).

[63] X. Roca-Maza, X. Viñas, M. Centelles, B. K. Agrawal, G. Colò, N. Paar, J. Piekarewicz, and D. Vretenar, Phys. Rev. C **92**, 064304 (2015).

[64] J. Birkhan, M. Miorelli, S. Bacca, S. Bassauer, C. A. Bertulani, G. Hagen, H. Matsubara, P. von Neumann-Cosel, T. Papenbrock, N. Pietralla, V. Yu. Ponomarev, A. Richter, A. Schwenk, and A. Tamii, Phys. Rev. Lett. **118**, 252501 (2017).

[65] P. Danielewicz, P. Singh, and J. Lee, Nucl. Phys. A **958**, 147 (2017).

[66] S. S. Bao, J. N. Hu, Z. W. Zhang, and H. Shen, Phys. Rev. C **90**, 045802 (2014).

[67] G. Baym, H. A. Bethe, and C. J. Pethick, Nucl. Phys. A **175**, 225 (1971).

[68] J. M. Lattimer, C. J. Pethick, D. G. Ravenhall, and D. Q. Lamb, Nucl. Phys. A **432**, 646 (1985).

[69] J. M. Lattimer and F. D. Swesty, Nucl. Phys. A **535**, 331 (1991).

[70] S. S. Avancini, D. P. Menezes, M. D. Alloy, J. R. Marinelli, M. M. W. Moraes, and C. Providência, Phys. Rev. C **78**, 015802 (2008).

[71] P. Rehberg, S. P. Klevansky, and J. Hüfner, Phys. Rev. C **53**, 410 (1996).

[72] P. B. Demorest, T. Pennucci, S. M. Ranson, M. S. E. Roberts, and J. W. T. Hessels, Nature (London) **467**, 1081 (2010).

[73] E. Fonseca, T. T. Pennucci, J. A. Ellis, I. H. Stairs, D. J. Nice, S. M. Ransom, P. B. Demorest, Z. Arzoumanian, K. Crowter, T. Dolch, R. D. Ferdman, M. E. Gonzalez, G. Jones, M. L. Jones, M. T. Lam, L. Levin, M. A. McLaughlin, K. Stovall, J. K. Swiggum, and W. Zhu, Astrophys. J. **832**, 167 (2016).

[74] J. Antoniadis, P. C. C. Freire, N. Wex, T. M. Tauris, R. S. Lynch, M. H. van Kerkwijk, M. Kramer, C. Bassa, V. S. Dhillon, T. Driebe, J. W. T. Hessels, V. M. Kaspi, V. I. Kondratiev, N. Langer, T. R. Marsh, M. A. McLaughlin, T. T. Pennucci, S. M. Ransom, I. H. Stairs, J. van Leeuwen, J. P. W. Verbiest, and D. G. Whelan, Science **340**, 1233232 (2013).